Journal Pre-proofs

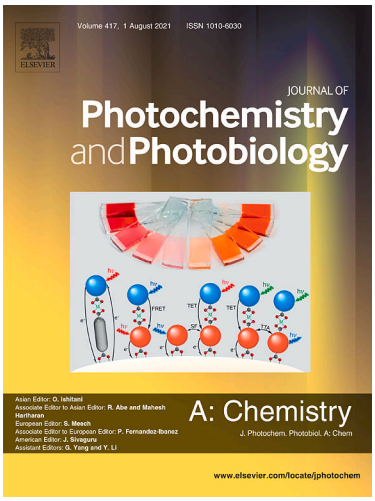

Photocatalytic performance of palladium and carbon modified TiO_2 using solar radiation

L. Rossi, P.I. Villabrille, L.M. Pastrana-Martínez, P. Caregnato, J.A. Rosso

PII: S1010-6030(22)00684-0
DOI: https://doi.org/10.1016/j.jphotochem.2022.114461
Reference: JPC 114461

To appear in: *Journal of Photochemistry & Photobiology, A: Chemistry*

Received Date: 25 August 2022
Revised Date: 27 October 2022
Accepted Date: 26 November 2022

Please cite this article as: L. Rossi, P.I. Villabrille, L.M. Pastrana-Martínez, P. Caregnato, J.A. Rosso, Photocatalytic performance of palladium and carbon modified TiO_2 using solar radiation, *Journal of Photochemistry & Photobiology, A: Chemistry* (2022), doi: https://doi.org/10.1016/j.jphotochem.2022.114461

Photocatalytic performance of palladium and carbon modified TiO_2 using solar radiation

L. Rossi[a], P. I. Villabrille[a], L. M. Pastrana-Martínez[b], P. Caregnato[c], J. A. Rosso[c,*]

[a] *Centro de Investigación y Desarrollo en Ciencias Aplicadas "Dr. Jorge J. Ronco" (CINDECA), Facultad de Ciencias Exactas, Universidad Nacional de La Plata, CCT La Plata–CONICET, La Plata, Argentina.*

[b] *NanoTech – Nanomaterials and Sustainable Chemicals Technologies, Department of Inorganic Chemistry, Faculty of Science, University of Granada, Granada, Spain.*

[c] *Instituto de Investigaciones Fisicoquímicas Teóricas y Aplicadas (INIFTA), Facultad de Ciencias Exactas, Universidad Nacional de La Plata, CCT La Plata–CONICET, La Plata, Argentina.*

**e-mail: janinarosso@gmail.com*

Abstract

TiO_2 photocatalysts were synthesized by the sol-gel method in the presence of Pd^{2+} ions and Tween 80. For each material, the effect of the synthesis conditions was studied by its characterization. Photoactivity was evaluated for the selective degradation of phenol (as model pollutant) with Aldrich humic acid (as usual interference) in the reaction mixture, using UV or visible lamps, and under natural sunlight. The materials were able to efficiently degrade phenol, even in the presence of humic acid in the mixture. The solar radiation experiment showed the outstanding photocatalytic activity achieved by TiO_2 modified with carbon and palladium: 74% of phenol degradation (70% of mineralization, without Pd leaching) after 5 h of exposure.

Keywords: Tween 80, Photocatalyst, Phenol, Humic acid, Solar exposure.

1. *Introduction*

TiO_2-based photocatalysts show a great potential for environmental remediation because of photocatalytic oxidation, which is activated under solar or UV light [1]. They have remarkable characteristics such as nontoxicity, exceptional thermal and chemical stability, and high photocatalytic degradation ability [2]. Nevertheless, TiO_2 applications pose some challenges

to organic effluents, such as particle aggregation, mass transfer limitation, high band energy, and scattering conditions [3].

The photocatalytic efficiency of TiO_2 could be increased through the modification by metal-ion doping [4], metal loading [5] and/or introducing a heterojunction [6]. In particular, palladium appears as a promising and versatile candidate to modify the TiO_2 photocatalyst, as reported by several publications [7,8,17,9–16].

On the other hand, the use of a surfactant is considered another strategy to improve the photocatalytic properties of TiO_2. The surfactant effect on phase-controlled synthesis and photocatalyst properties of TiO_2 nanoparticles was studied [18–23]. Results indicated the stability, size, and shape of surfactant micelles were the main factors to determine TiO_2 phase. The anatase phase was found when the micelle was small and stable. The bigger nanoparticles of various sizes were obtained in the non-surfactant system because there was no limit to crystal growth during the reaction, whereas, when using a surfactant, smaller nanoparticles of uniform size were produced with the control of the micelle space and shape. In addition, surfactant lowers the energy required to increase the interfacial area and form smaller nanoparticles. Several publications described the modification of the TiO_2 inorganic network by following a sol–gel method modified with surfactants, in particular, nonionic surfactant of the Tween series [20–22,24]. Chen and coworkers reported that the increment of surfactant loading led to an improvement in Brunauer-Emmett-Teller (BET) specific surface area, pore volume/porosity, UV light absorbance, and photocatalytic performance [20]. Particularly, Tween 80 is a hydrophilic nonionic surfactant that has high solubilizing ability and is also a well-known emulsifier [25]. It could help to dissolve and stabilize the ethanol:water synthesis mixture containing the metal TiO_2 modifier precursor. Its presence could also help the synthesis ingredients to mix and prevent the separation of the particles. As a result, it is expected that its use could lead to better control of the morphology of the resulting TiO_2 modified photocatalysts.

Therefore, to improve the performance of the TiO_2 photocatalyst, both palladium modification and the addition of Tween 80 were tested during the sol-gel synthesis.

Domestic and industrial effluents release harmful and toxic phenolic compounds into water bodies, so the degradation of phenol and its derivatives has become a major global concern [3]. Moreover, phenol is frequently studied as a model pollutant due to its known degradation mechanism [26–29]. For TiO_2-based photocatalysts, the hydroxyl radical ($^{\cdot}OH$) is known to be the primary oxidant in an aqueous solution [30,31]. The reaction between phenol and $^{\cdot}OH$ produces hydroquinone, catechol, and p-benzoquinone as the main intermediates. Then, these compounds can be attacked by $^{\cdot}OH$, reaching complete mineralization, and

thus producing CO_2 and H_2O [32]. For these reasons, the photocatalytic degradation of phenol is useful to evaluate materials and to scan the most favorable operating conditions.

Natural organic matter (NOM), a key component in aquatic environments, is a complex matrix of organic substances characterized by its variable molecular and chemical properties [33]. The NOM concentration found in most natural waters varies between 0.1 and 20 mg L^{-1} [34]. Dissolved ~~natural organic matter~~ NOM in water bodies ~~is a major limiting factor: it~~ causes a significant inhibitory effect on the micropollutant removal performance of TiO_2 photocatalysts [2,24,34–41]. Particularly, the interference of humic substances (HS) has been reported [24,38,39]. In natural waters, HS represent the most important fraction of colored dissolved ~~organic matter~~ NOM that absorbs solar radiation, they play a key role in aquatic photochemistry, and therefore they must be considered to evaluate the performance of photocatalysts. Then, the degradation of phenol in the presence of a commercial humic acid (Aldrich) was assayed with the synthesized photocatalysts.

The goal of this work is the preparation of TiO_2 photocatalysts by the sol-gel method in the presence of Pd ions and Tween 80. The effect of the synthesis conditions on the characteristics of each material was investigated, and its photoactivity was evaluated for the selective degradation of phenol in the presence of Aldrich humic acid (AHA) using UV and visible light. Furthermore, experiments were carried out to explore its performance using solar irradiation, as an ecological and cost-effective alternative.

2. *Material and methods*

2.1. Preparation and characterization of catalysts

The sol-gel method was employed to prepare the catalysts. Titanium(IV) isopropoxide (TTIP, Aldrich) and palladium(II) acetylacetonate ($Pd(acac)_2$, Aldrich) were used as metal-ion precursors. The required amount of $Pd(acac)_2$ was dissolved in distilled water and ethanol (EtOH, Soria) before TTIP hydrolysis. The procedure was based on our previous work [39] using a TTIP:EtOH:H_2O:HNO_3 molar ratio of 1:40:169:0.1. A synthesis was carried out with the addition of nonionic surfactant Tween 80 (Tw) using a Tw:TTIP ratio of 0.03:1, following a similar procedure to our previous work [38]. The material obtained with 0.10 at. % of Pd was called 0.10Pd-TwT. Titania with and without Tw, named TwT and T, respectively, was similarly prepared for comparison purposes. For all cases, the crystals obtained were ground to powder and calcined at 400 °C (6 °C min^{-1}) for 1 h.

X-ray diffraction (XRD) was used to examine the crystal structure patterns of the powder samples by a PANalytical X'Pert Pro diffractometer (with Cu Kα radiation). BET surface area measurements were carried out by N_2 physisorption with Micromeritics ASAP 2020

adsorption analyzer. UV-Vis diffuse reflectance spectra (DRS) were obtained with a UV–Vis PG Instrument Ltd. T90 spectrophotometer. Fourier transform infrared (FTIR) spectra were analyzed on KBr pellets of the samples (in the range of 4000 and 400 cm^{-1}), at room temperature, using a BRUKER Vertex 70 spectrometer.

Photoluminescence (PL) lifetime measurements of T, Tw, and 0.10Pd-TwT particles suspended in water were carried out on a JOBIN-YVON SPEX FLUOROLOG FL3-11 with lifetime, time-correlated single photon counting (TCSPC) with LED excitation at 295 nm. Time-resolved emission spectroscopy (TRES) was performed at the same excitation wavelength.

The electron microscopy analysis was carried out using a TALOS F200A transmission electron microscope (TEM), designed for high-resolution imaging.

The surfaces of 0.10Pd-TwT were analyzed by X-ray photoelectron spectroscopy (XPS), using a Kratos Axis Ultra-DLD instrument. This study was carried out with a monochromatic Al Kα X-ray as radiation source (~~15 kV, 90 W~~ hν = 1486.6 eV) ~~with a 20 eV pass energy for regions and 160 eV for survey.~~ and hemispherical electron analyzer. Survey and multi-regio spectra were recorded at C1s, O1s, Ti2p and Pd3d photoelectron peaks. ~~The analysis was performed at a pressure of 100 nPa.~~ The binding energy (BE) values were taken from the guide of the equipment and referred to the C1s line of the adventitious carbon, at 285.0 eV.

2.2. Lamp irradiation tests

A Rayonet photoreactor RPR-100 (Southern New England Ultraviolet Company) with interchangeable lamps (UV or visible) was employed. The emission spectra of the lamps were previously reported [42]. A cylindrical glass tube was used to contain the mixture reaction in air at 25 °C with continuous magnetic stirring. A reaction mixture of phenol (50 μM) in ultrapure water (Milli-Q: resistivity >18 MΩ cm and <20 ppb organic carbon) and photocatalyst (1 g L^{-1}) was ultrasonically dispersed and kept in the dark for 15 min before turning on the lamps. In addition, for some experiments, 12 mg L^{-1} of AHA was also added to the reaction mixture. The initial concentration of AHA was chosen according to the generally reported average value [34,38]. All tests were carried out at the intrinsic pH of the mixture (around 5).

Samples were collected periodically, filtered through a 0.45 μm pore size cellulose membrane, and stored in amber glass bottles at 4°C until analysis.

An HPLC, HP1050 Ti series, and the corresponding standard solutions were used to estimate the phenol concentration in the samples. A reversed-phase C18 (4.6 mm, 250 mm, 5 μm) Restek Pinnacle II was used as column with a 50/50 (v/v) CH_3OH/H_3PO_4 (0.1%)

solution as eluent at a flow rate of 0.8 mL min^{-1}. To avoid any interference in the HPLC determination, the AHA was removed from the samples according to the procedure previously reported [38]. The total carbon (TC) was measured by a high-temperature carbon analyzer model TOC 5000A from Shimadzu. The detection limit was 1 ppm of C. These determinations were carried out for a more effective estimation of the degree of mineralization considering all the organic compounds in the reaction medium.

To evaluate photolysis of phenol and AHA, control assays were performed. For this purpose, the evolution of phenol concentration and the degree of mineralization in aqueous solution with irradiation (without catalyst) were analyzed. The adsorption of phenol and AHA on the materials was also checked, monitoring the evolution of the concentration of phenol and TC without irradiation (with each catalyst).

2.3. Solar photocatalytic experiments

For these tests, 250 mL discontinuous cylindrical glass reactors (9 cm diameter) were used under continuous stirring. The reaction mixture containing 100 mg of the selected catalyst (1 g L^{-1}), with the required amounts of phenol (250 μM) and AHA (12 mg L^{-1}), was ultrasonically dispersed in 100 mL of ultrapure water in each experiment. Based on our previous experience [42], the initial concentration of phenol was five times higher than that used in the lamp experiments. The mixtures were kept in the dark for 15 min to reach adsorption/desorption equilibrium.

Solar exposure experiments were conducted in the summer period of the Southern Hemisphere. The reaction mixtures were exposed to sunlight on a horizontal platform located in La Plata City, Argentina (34.90° S, 57.92°W, 15 MASL). The local time (LT) is given by universal time minus 3 h, and solar noon ranged from 12:39 p.m. to 01:05 p.m. in the geographical position and seasons established. The reaction mixtures were exposed in clear-sky days, for a period of 5 h, centered on solar noon. The transmittance of the glass covering the reactor was previously quantified, allowing radiation of $\lambda > 310$ nm to pass. Solar irradiance data were recorded every 15 min using 5.0 Solarmeter and 10.0 Solarmeter radiometers for the UV (280-400 nm), and visible and near IR (400-1100 nm) regions, respectively. These data were analyzed as described in a previous publication [42].

The samples were taken periodically, and stored as previously mentioned, until their analysis by HPLC and TOC. To estimate palladium leaching from the catalysts at the end of the irradiation period, the metal concentration in the final solution was determined by inductively coupled plasma mass spectrometry (ICP-MS, Nexlon 300X, Perkin-Elmer Co.).

The direct photolysis of phenol and AHA was evaluated without catalyst under the same experimental conditions.

3. Results and discussion

The XRD patterns observed for T, TwT, and 0.10Pd-TwT revealed the presence of anatase as the TiO_2 crystalline phase for the following 2θ values: 25.2°, 37.8°, 48.0°, 54.0°, and 54.9° (as shown in **Figure 1**). From the diffraction peak broadening and using the Scherrer equation [43], the average size of primary anatase crystallites was estimated (see **Table 1**). No evidence of large domains of PdO was found for 0.10Pd-TwT.

The presence of Tw in the synthesis led to a reduction in the crystallite size. Wiranwetchayan and coworkers claimed that the presence of a polymeric precursor in the synthesis could play a role in the hydrolysis, condensation and microstrain, leading to a decrease in the TiO_2 crystallite size [44]. Moreover, Lee and coworkers reported that the crystallite size decreased from 12 to 9 nm with increasing chain length of the hydrophobic group, when using the Tween series [21].

The addition of Pd in the presence of Tw also led to a decrease in the average crystallite size. A similar trend was described by other researchers [12,45,46]. The smaller crystal size with an increase in the Pd content can be caused by a reduction in particle nucleation during hydrolysis/condensation of TTIP or by a decrease in grain boundaries during the sintering process, due to the presence of Pd^{2+} ions [12,46].

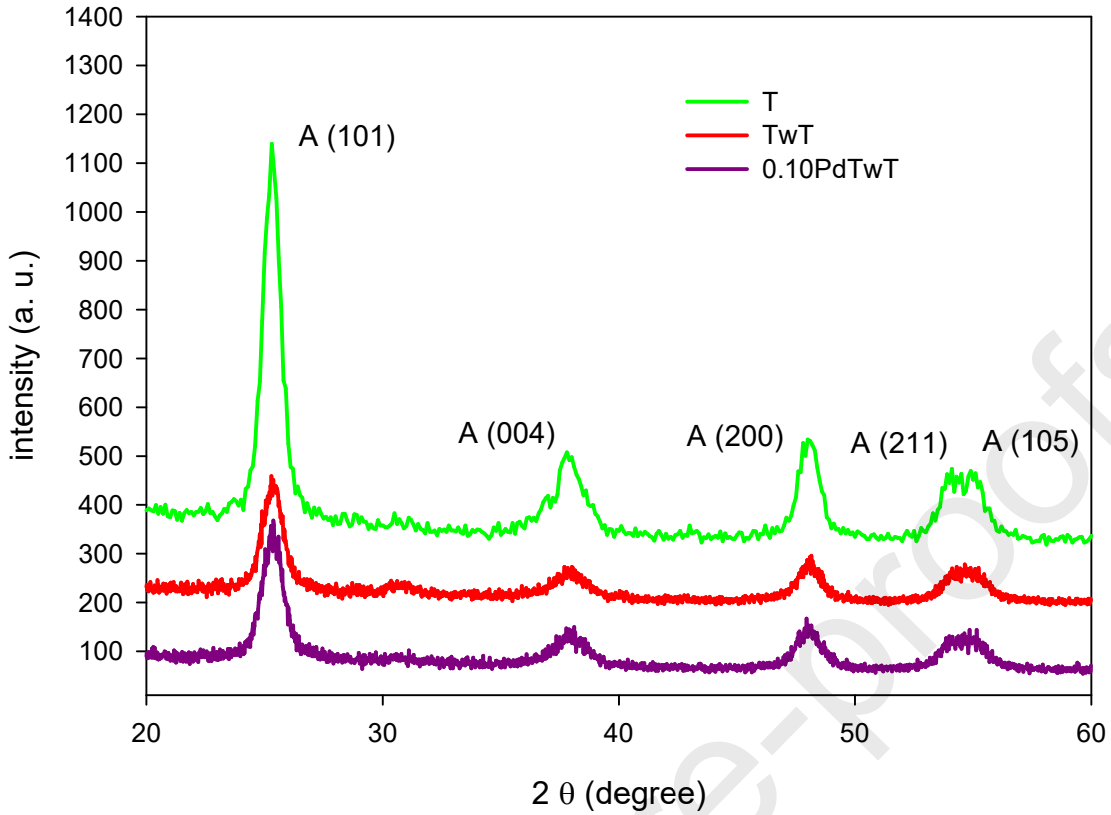

Figure 1. XRD for the synthesized catalysts T, TwT, and 0.10Pd-TwT. A: anatase.

Table 1 Structural and textural properties of the materials synthesized.

Sample	Anatase crystallite size (nm)	BET specific surface area ($m^2\ g^{-1}$)	BJH total pore volume ($cm^3\ g^{-1}$)	BJH average pore diameter (nm)	E_{BG} (eV)
T	10.01	88	0.12	4.4	3.01
TwT	9.18	102	0.16	4.7	3.07
0.10Pd-TwT	8.04	103	0.15	4.8	2.77

The N_2 adsorption-desorption isotherms of T, TwT, and 0.10Pd-TwT are presented in **Figure 2**. The type of isotherm and hysteresis loop is the same in all cases, Type IVa isotherm with H2b hysteresis loop according to the IUPAC classification [47] indicating mesoporous materials [48]. The textural properties estimated from the isotherms are listed in **Table 1**. Comparing the properties of T and TwT, an increase in the surface area, volume, and pore size of the material appears as a consequence of the addition of Tw during synthesis. It could be assumed that this nonionic surfactant with a long hydrophobic tail (C17) inhibited both the growth of crystallites and the aggregation of adjacent primary particles [38]. No effect was observed with the addition of Pd, since TwT and 0.10Pd-TwT have similar textural properties, as can be seen in **Table 1**.

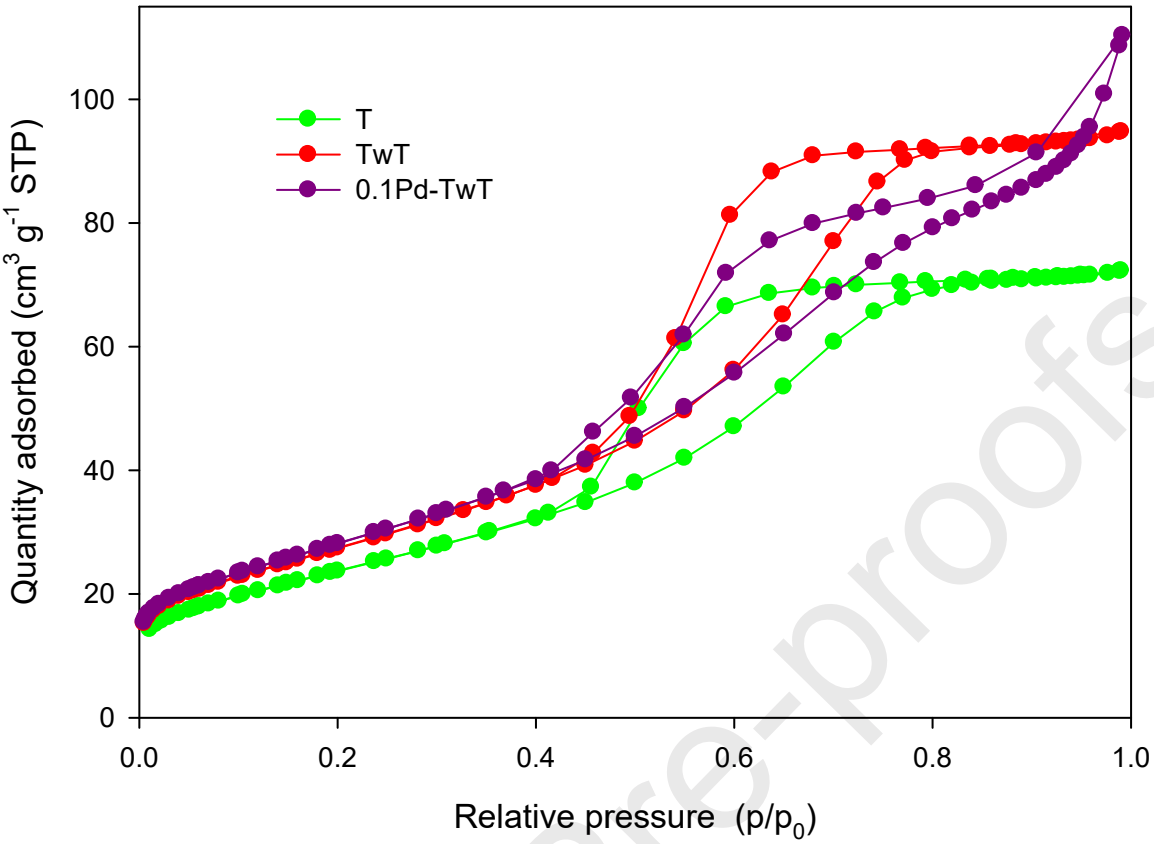

Figure 2: N_2 adsorption-desorption isotherms for T, TwT, and 0.10Pd-TwT

UV–vis diffuse reflectance spectra and Tauc plots for T, TwT, and 0.10Pd-TwT are shown in **Figure 3**. All materials showed strong and broad absorption below 400 nm due to a charge-transfer transition between the lattice oxygen ligands and an octahedrally coordinated titanium ion. Additionally, an important variation in the absorption in the visible region for TwT could be observed. Several publications related this behavior to the presence of carbon on the TiO_2 surface [20,44,49–53]. Remarkable light absorption in the visible region was reported for carbon-deposited TiO_2 nanoparticles prepared using glucose as the carbon source [52]. The absorbance of the TiO_2 nanoparticles covered by a carbonaceous layer is enhanced at a wavelength of 400-800 nm after increasing the carbon content. In our case, it is likely that carbon residues remain on the TwT surface even after calcination, causing this increase in its absorption. The incorporation of palladium (0.10Pd-TwT) induces a broad band between 450 and 600 nm, which could be assigned to a d–d transition of PdO particles, as widely reported [7–9,54–58].

The band gap energies of TiO_2 materials could be estimated using the Kubelka–Munk theory for the indirect allowed transition [59]. The values of T and TwT were similar, with an average value of 3.04 ± 0.03 eV, while the value of 0.10Pd-TwT was lower, 2.77 eV.

Several metal-based modifications of TiO_2 have been proposed to improve its photocatalytic efficiency [4–6]. A semiconductor heterojunction involves a combination of two semiconducting materials with different band structures, with no relevant changes in band gap energies [6]. Meanwhile, doping is the term that refers to the introduction of ionic species in the crystal lattice of a semiconductor, leading to a change in band gap energies [4]. Although metal ions could join the TiO_2 lattice (in interstitial or substitutional mode), the size of Pd^{2+} (86 pm) is larger than that of Ti^{4+} (60.5 pm), indicating that doping was unlikely. Therefore, if the Pd remains as Pd^{2+}, the semiconductor heterojunction is more likely than doping. However, based on the observed decrease in the band gap energy of 0.10Pd-TwT, doping could not be completely ruled out.

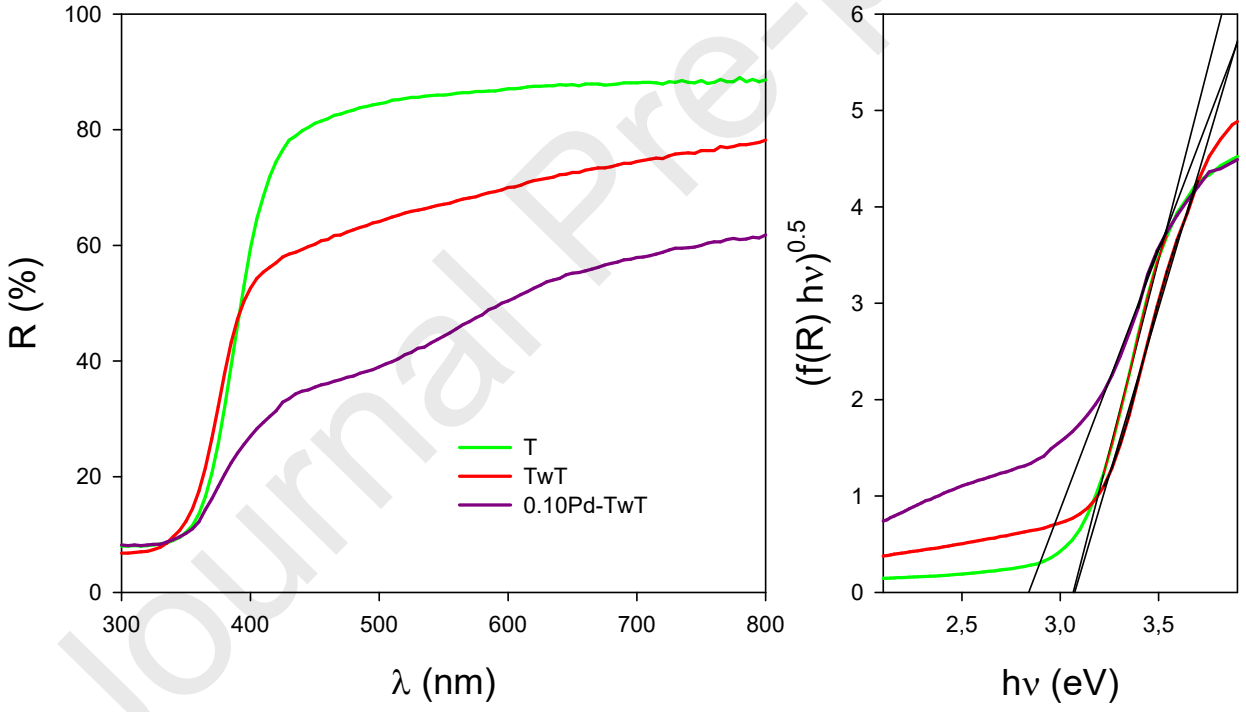

Figure 3. UV-visible DRS for the synthesized catalysts T, TwT, and 0.10Pd-TwT, and the corresponding Tauc plots for band gap energy determinations.

Time-resolved PL measurements were done at wavelength emission ($\lambda_{em.}$) of 360 nm for T, TwT, and 0.10Pd-TwT samples, and the experimental curves were fitted with three (n=3) exponential decay functions, using Eq. 1. The fitted parameters α_i and τ_i (pre-exponential factor and lifetime, respectively) are shown in **Table 2**. **Figure 4** depicts the time-

dependence of 0.10Pd-TwT luminescence where the red line is the best fit employing Eq. 1.

Table 2. Best fitted parameters of three exponential components using Eq. 1-3.

Sample name	Pre-exponential functions			Decay lifetimes (ns)				Fractional contributions			
	α_1	α_2	α_3	τ_1	τ_2	τ_3	$\tau_{av.}$	f_1	f_2	f_3	goodness of fit parameter (X^2)
T	9.0e-3	3.8e-4	7.3e-5	1.0	5.1	18.5	3.6	73.2	15.8	11.0	1.005432
Tw	9.2e-3	4.9e-4	1.2e-4	1.0	4.8	16.8	4.0	67.5	17.3	15.1	1.09999
0.10Pd-TwT	9.6e-3	2.9e-4	1.5e-4	1.0	5.0	15.1	3.8	73.7	9.2	17.1	1.124837

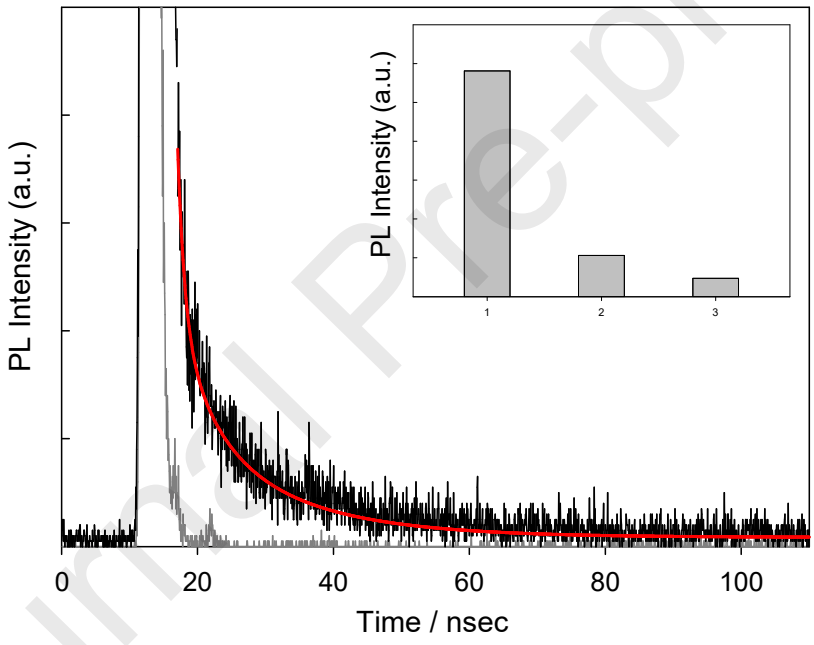

Figure 4. PL decay profile of 0.10Pd-TwT (black line). The grey and the red lines represent the prompt and fit using Eq. 1, respectively. Inset: PL contribution at $\lambda_{em.}$= 350 nm (λexc= 295nm) obtained from TRES analysis for 0.10Pd-TwT sample.

The PL dynamics involves a dominant very fast (1 ns) relaxation with lifetime τ_1, and two relatively longer-lasting emissions with lifetimes τ_2 and τ_3. The last one is on the order of tens of nanosecond.

Several authors [60–62] have proposed that the fast relaxation, τ_1, is related to radiative recombination of the photogenerated charge carriers in the band edge. Also, another group of the charge carriers relaxes to the shallow-trap levels, which radiatively recombine with the lifetime of τ_2. The rest of the photogenerated charge carriers could be relaxed to the

deep-trap levels and consequently, recombine radiatively with a much longer lifetime of τ_3. Shallow and deep trap levels are related to distortion of TiO_2 lattice and oxygen vacancies of the nanostructure.

The average decay time, τ_{av}, calculated using Eq. 2, increases for the TwT and 0.10Pd-TwT samples, as compared to the T nanostructure.

The value of *fi*, calculated from Eq. 3, is the fractional contribution of each emission associated with τi. By comparing *fi* values from Table 2, it is found that $\%f_2$ and $\%f_3$ of the lifetimes τ_2 and τ_3 corresponding to the defect-related emissions increase in the TwT sample compared to pristine TiO_2 results.

$$I(t) = b + \sum_{i=1}^{n} \alpha_i exp\,(-t/\tau_i) \qquad \text{Eq. 1}$$

$$\langle \tau \rangle = \frac{\sum_{i=1}^{n} \alpha_i \tau_i^2}{\sum_{i=1}^{n} \alpha_i \tau_i} \qquad \text{Eq. 2}$$

$$f_i = \frac{\alpha_i \tau_i}{\sum_{j=1}^{n} \alpha_j \tau_j} \qquad \text{Eq. 3}$$

The same behavior is observed with f_3 for 0.10Pd-TwT sample. Nevertheless, f_2 contribution decreases in 0.10Pd-TwT when compared with T and TwT ones.

The present results confirm that the presence of Pd and/or Tw in the synthesis media mainly affects the density of trap states, which is correlated with f_2 and f_3 values. This explains the longer lifetime observed for TwT and 0.10Pd-TwT nanostructures compared to that of T.

TRES was performed at the same excitation wavelength. The emission spectrum associated with each lifetime may be obtained by taking the contribution of each decay lifetime to the overall emission at a given wavelength. The inset in **Figure 4** exhibits the 0.10Pd-TwT PL intensity contribution at $\lambda_{em.}$= 350 nm for each of the three components of the decay, using Eq. 1. Das and coworkers demonstrated that PL emissions close to 350 nm in TiO_2 nanostructure corresponded to the near band edge emissions [60]. Besides, in the doped samples PL intensity at this wavelength was quenched, which was attributed to the nonradiative transitions to deep trap states.

Summing up, in our experiments the PL emission spectrum of each contribution associated with τ_1, τ_2 and τ_3 demonstrates that the first contribution (species 1) has the largest emission at 350 nm. Meanwhile, the second and third contributions (species 2 and 3) significantly decrease the emission related to near band edge transitions.

FTIR spectra of T and TwT samples were analyzed (**Figure 5**). They show the strongest broad band between 900 and 400 cm^{-1}, which indicates the stretching vibration of the Ti-O-Ti bonds of the TiO_2 lattice [63]. The broad band at around 3400 cm^{-1} is assigned to O–H stretching vibration. It could correspond to physisorbed H_2O [64] and/or Ti-OH bonds [21]. Physisorbed water was also evidenced by the band at ca. 1630 cm^{-1}, attributed to its H-OH stretching vibration [22]. The subtraction between both FTIR spectra (TwT minus T) reveals bands that are attributed to organic polymer residues, even after the calcination treatment. They are in the range 1700-1550, 1470-1350, and 950-850 cm^{-1} and are assigned to C=O, C=C, and C-O-C bonds, respectively [44,53]. Therefore, due to the addition of Tw during the synthesis, the presence of some carbon residues in the material obtained (TwT) was evidenced.

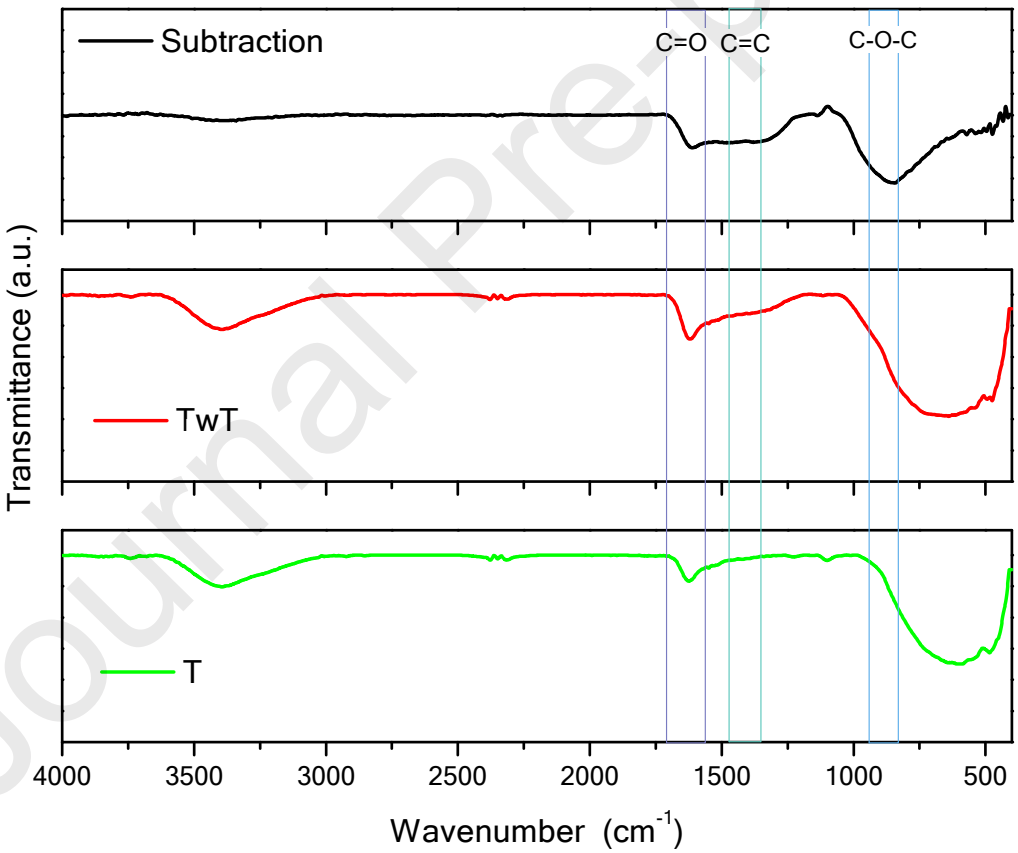

Figure 5. FTIR spectra of TwT and T samples, and their subtraction.

Figure 6 shows TEM micrographs for TwT and 0.10Pd-TwT catalysts. In the areas marked **a1** and **b1**, the lattice fringes can be clearly distinguished. The crystalline planes of anatase, (101) and (004), were identified according to the d-spacing values, 0.34 and 0.23 nm,

313 respectively. Additionally, lattice spacings of 0.28 nm and 0.22 nm were measured in area
314 **b1**. They were assigned to lattice planes of tetragonal PdO, (002) and (110), respectively
315 [65], providing further evidence of PdO formation on the surface of 0.10Pd-TwT.
316 Additionally, **Figure 6** shows a bright thin layer around the particles for materials synthesized
317 with Tween 80. Moreover, an amorphous layer with a thickness of around 0.48 nm can be
318 distinguished in **Figure 6.a1 and 6.b1** (see black rows).
319 Carbon layer formation has already been reported using different carbon precursors and
320 varying calcination conditions [66,67]. Ye and coworkers prepared a photocatalytic
321 composite material that consisted of an amorphous carbon layer between two
322 semiconductors, using glucose as carbon source [66]. They reported an amorphous C layer
323 of around 10 nm according to TEM images. In another publication, the surface carbon layers
324 on Pt/TiO_2 catalysts were achieved by using Tween 40 as part of the carbon precursor [67].
325 Moreover, TEM micrographs showed different thicknesses of carbon layers caused by
326 calcination in argon, air or oxygen atmosphere.
327 In our case, as shown by FTIR and DRS spectra, calcination for 1 h may not remove all the
328 Tween 80 used. Thus, the observed amorphous layer (**Figure 6a and 6b**) may well be a
329 residual C layer formed after using Tween 80 as a modifier during the synthesis of the
330 semiconductor materials.
331

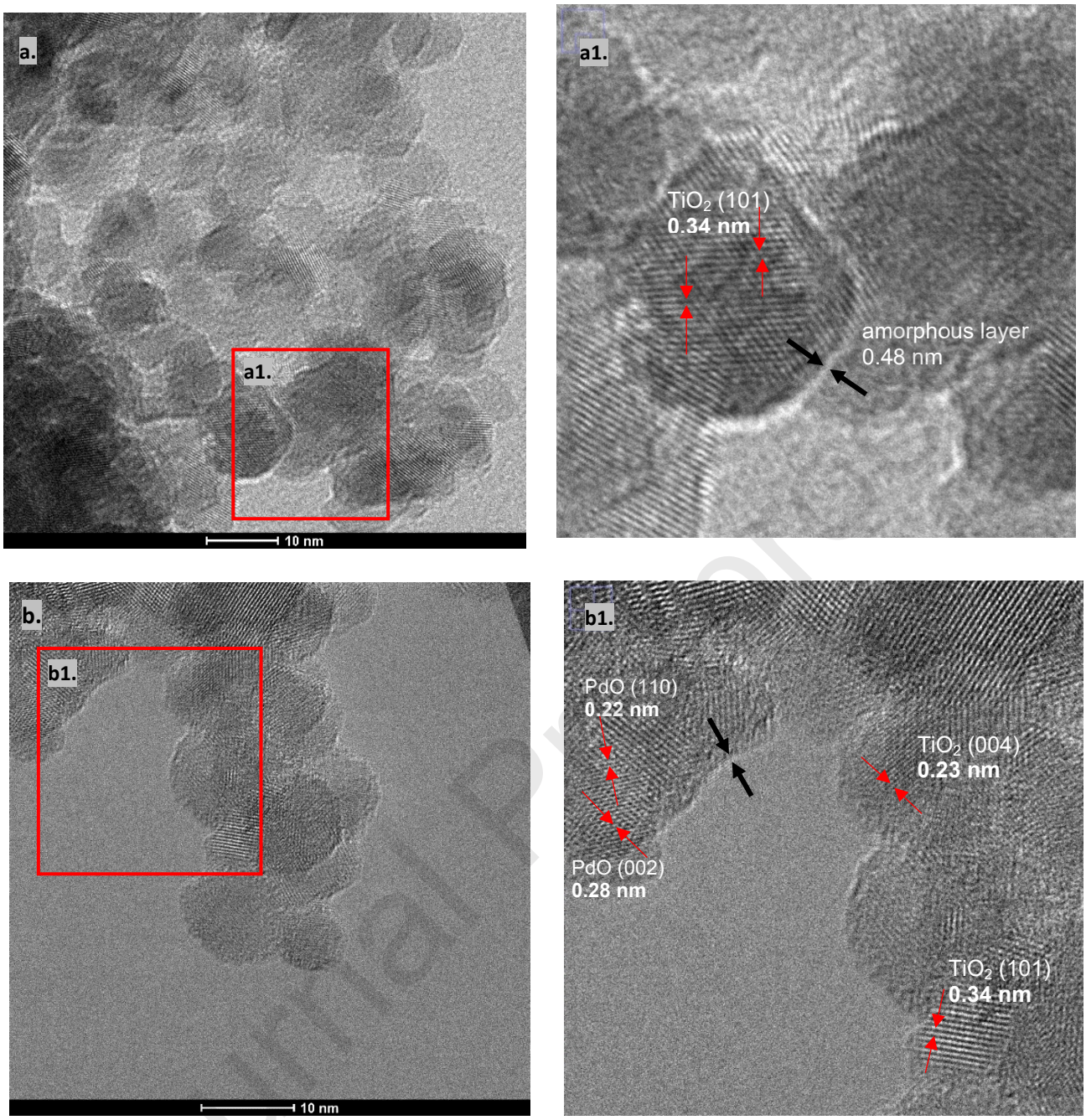

Figure 5. TEM micrographs of (**a**) TwT and (b) 0.10Pd-TwT, with (a1) and (b1) zones, respectively, to visualize some lattice fringes of TiO_2 and PdO.

The XPS analysis for 0.10Pd-TwT is presented in **Figure 7**. Ti 2p spectra (**Figure 7.a**) revealed two components for Ti $2p_{3/2}$ after deconvolution. Their BE values were estimated at 457.4 and 458.8 eV, attributed to the titanium oxidation states Ti^{3+} and Ti^{4+}, respectively [68]. The main contribution, 95%, corresponded to Ti^{4+}. The peak located at ca. 464.5 corresponding to Ti $2p_{1/2}$.

The Pd 3d was observed within the 334 - 346 eV region (**Figure 7.b**) with two well-defined doublets of Pd $3d_{5/2}$ and Pd $3d_{3/2}$ [11]. These peaks were deconvoluted into two components

assigned to Pd^{2+} (73%, 336.4 and 341.6 eV) and Pd^{4+} (27%, 337.3 and 342.8 eV) based on previously reported values [11,69,70]. No metallic Pd was observed in this analysis.

The main component was Pd^{2+}, indicating the presence of PdO on the material surface. However, the observation of Pd^{4+} cannot be neglected. The Pd^{4+} size is similar to that of Ti^{4+}, 61.5 and 60.5 pm, respectively, increasing the possibility of doping (interstitial or substitutional mode). The doping of TiO_2 with Pd^{4+} could be responsible for the difference observed in the band gap energy for 0.10Pd-TwT (2.77 eV), which was lower than the values for the materials without Pd.

Figure 7.c shows the O 1s region. Three peaks at 530.1, 530.7, and 532.1 eV were fitted. The components at 530.1 and 532.1 eV were ascribed to the Ti-O linkages of TiO_2 and to the presence of Ti-OH bonds, respectively. This was based on the values reported by Zhong and coworkers, 529.6 eV and 532.0 eV [52]. These authors also reported a peak at 531.3 eV, assigned to C=O and/or COO species. Due to the existence of carbon residues detected by DRS, FTIR, and TEM on the surface of our materials, the component at 530.7 eV may be assigned to oxygen bonded to carbon species.

In **Figure 7.d**, the C 1s region is displayed. Three peaks were fitted at 285.0 eV (85%), 286.7 eV (8%), and 289.0 eV (7%). Based on the values reported by several authors [52,71,72] the main contribution at 285.0 eV was ascribed to the C-C or C-H carbon bonds, adventitious carbon contamination adsorbed from the ambient environment, while the contributions at 286.7 and 289.0 eV were due to C-OH (or C-O-C) and C=O (or COO), respectively.

These observations are in agreement with our DRS, FTIR, and TEM findings, which indicated that the addition of Tw during the synthesis under the described conditions resulted in the presence of some carbon residues in the materials obtained.

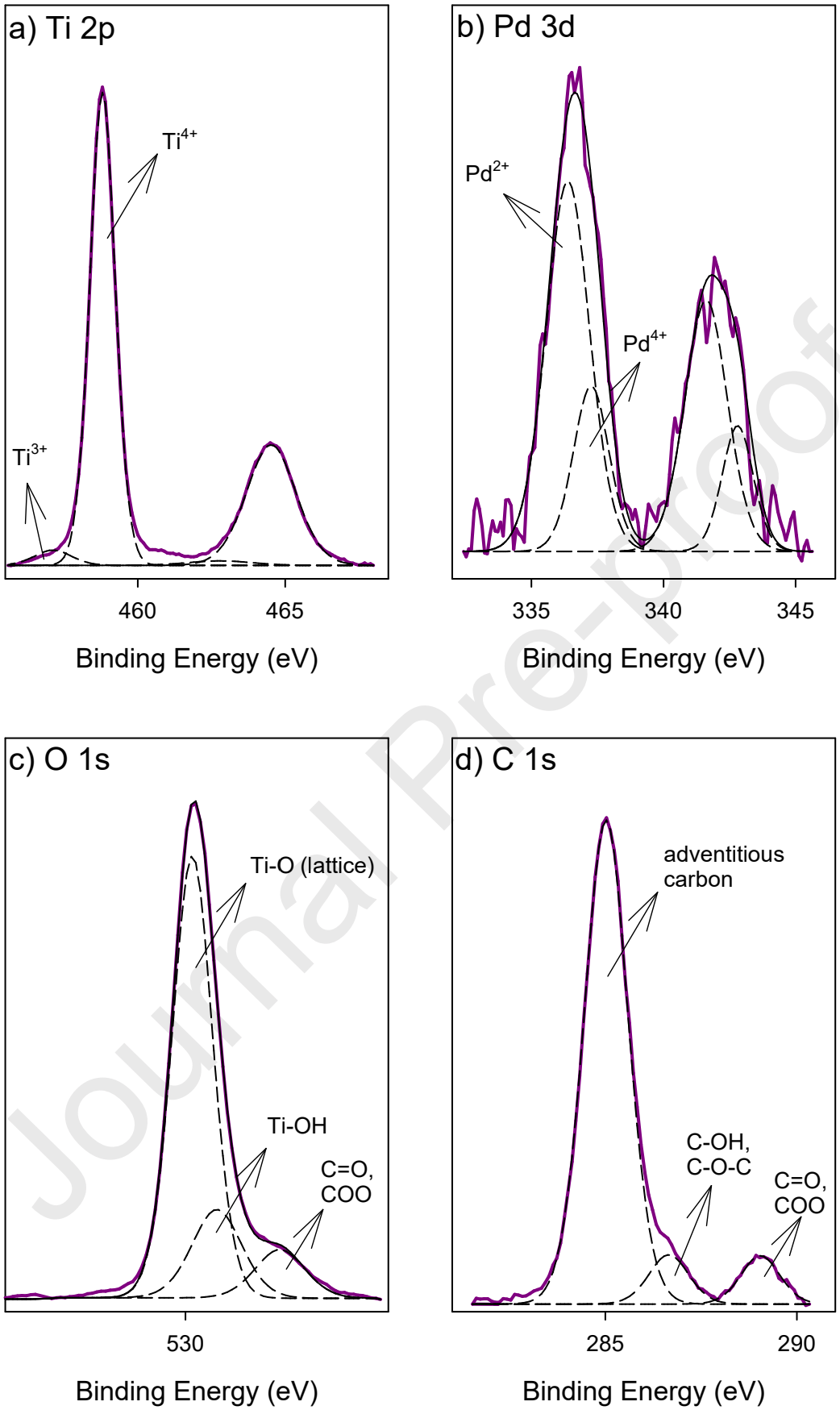

Figure 7. XPS scans for 0.10Pd-TwT catalyst for the regions: a) Ti 2p; b) Pd 3d; c) O 1s; d) C 1s. Solid lines correspond to the signals and dashed lines to fitting by deconvolution analysis.

The materials T, TwT, and 0.10Pd-TwT were assayed for phenol degradation for 2 h under UV lamp irradiation and for 5 h under visible lamp irradiation (**Figure 8**).

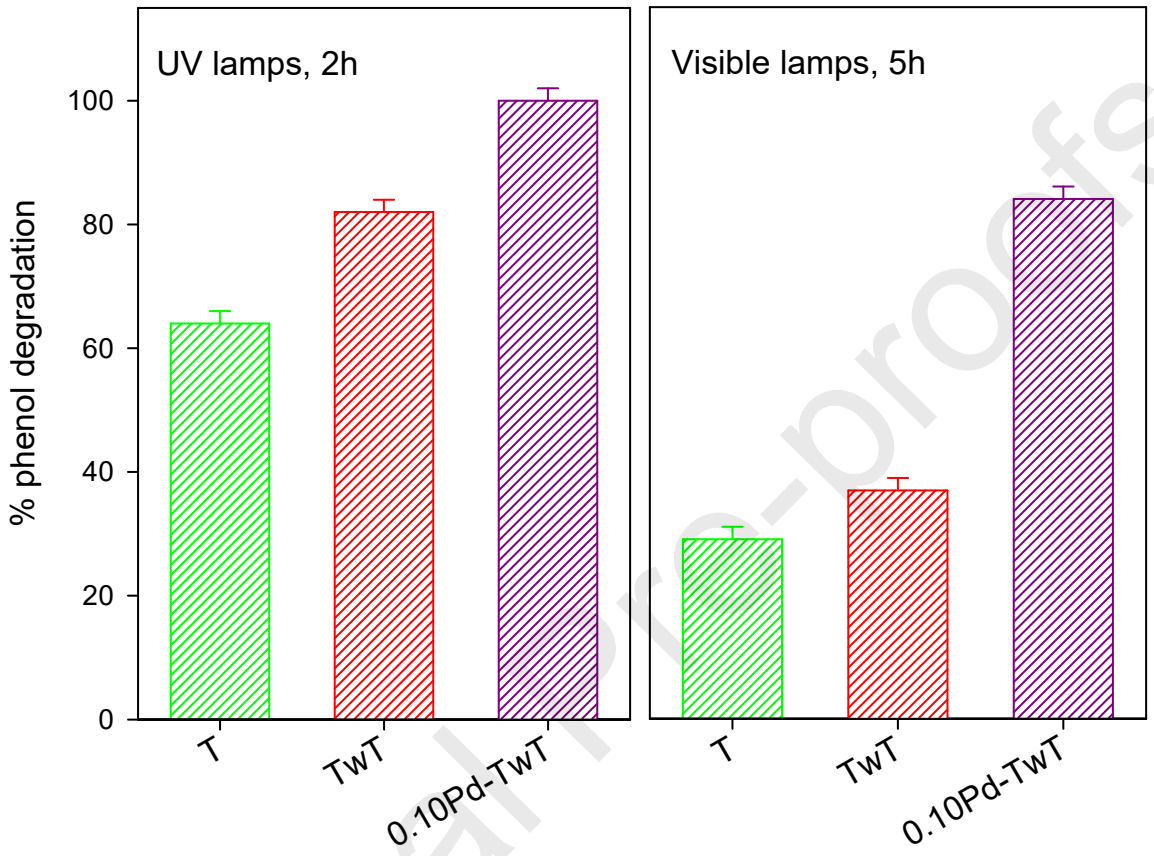

Figure 8. Effect of the use of Tween 80 and Pd^{2+} during the synthesis of materials on the photocatalytic degradation of phenol ($[phenol]_0$= 50 μM, 1 g L^{-1} catalyst).

For both irradiation conditions, TwT showed a better performance than T. Several publications described the enhancement in photocatalytic activity due to the presence of carbon on TiO_2 [20,49,51,52,72]. Chen and coworkers reported that increasing the Tween 20 loading in the sol improved the photocatalytic activity of the TiO_2–P25 composite films, and attributed this behavior to the increase in BET surface area and in the amount of crystalline materials (film weight) on the support [20]. For our TwT material, the increment in the BET surface area (from 88 m^2 g^{-1} for T to 102 m^2 g^{-1} for TwT) may well be considered as the principal reason for the enhancement of the photocatalytic activity.

On the other hand, 0.10Pd-TwT showed the best performance under UV and visible irradiation, 100 ± 2% and 84 ± 2% phenol degradation, respectively. It could be assumed

that doping with Pd^{4+} ions would favor the absorption of radiation at a higher wavelength and that the existence of PdO domains would favor the separation of charge carriers, as reported by Ismail and coworkers [73].

The better performance of TwT and 0.10Pd-TwT compared with pure TiO_2 in T samples was confirmed by the higher charge separation efficiency and the increase in the long-living photogenerated charge carriers, as was demonstrated in the time-resolved PL experiments by the comparison of the average lifetime $\tau_{av.}$ and f_3 values in **Table 2**. The presence of lattice defects, distortions and heterojunctions clearly supports the performance for the photocatalytic degradation of phenol.

The possibility of 0.10Pd-TwT reuse was checked by performing the degradation of phenol with UV lamps for 2 h. The values were 100%, 89% and 84% for the consecutive experiments, showing the good stability of this material throughout different cycles.

The effect caused by the presence of AHA in the reaction mixture on the photocatalytic degradation of phenol was tested. **Figure 9** shows the time-dependent evolution of phenol concentration using T, TwT, and 0.10Pd-TwT under UV irradiation, and TwT and 0.10Pd-TwT under visible irradiation.

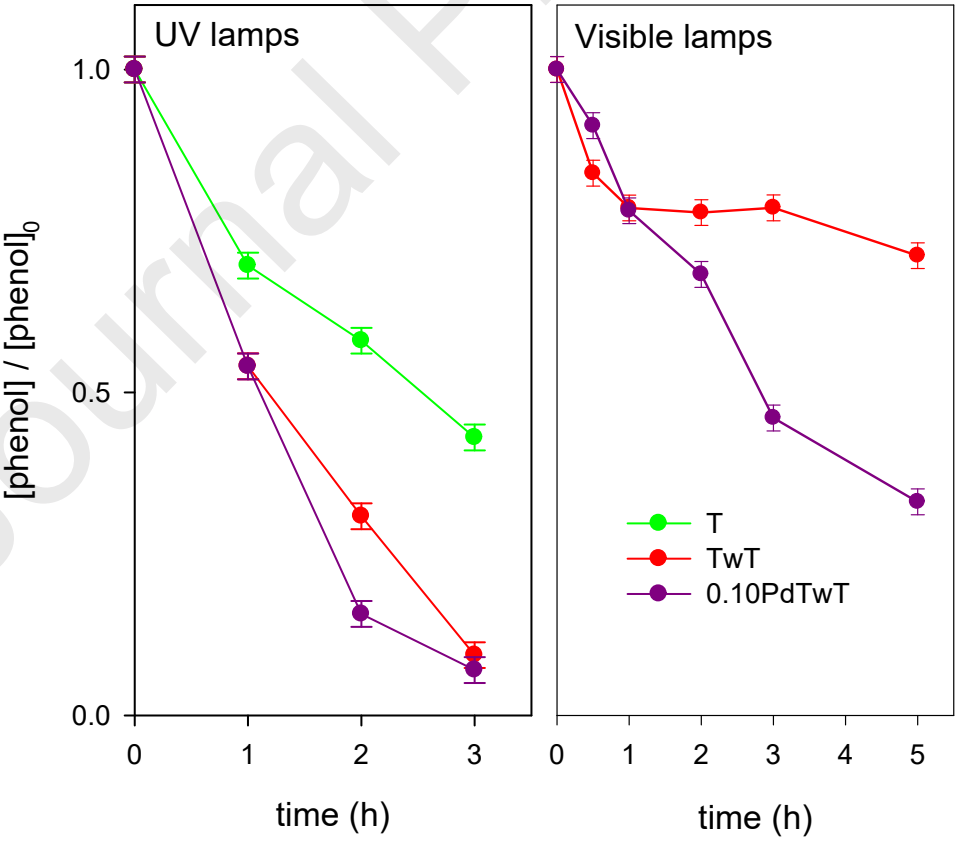

Figure 9. Time evolution of phenol concentration in the presence of a commercial humic acid by irradiation with UV or visible lamps, using T, TwT, and 0.10Pd-TwT (1 g L^{-1} catalyst).

434 $[phenol]_0$= 50 μM, $[AHA]_0$= 12 mg L^{-1}.
435
436 The photocatalytic activity of T led to 57 ± 2% degradation of phenol after 3 h under UV
437 irradiation. It should be noted that the degradation of phenol was lower than that in the
438 experiments without AHA (64 ± 2% after 2 h) but higher enough to consider the material as
439 an acceptable photocatalyst. Better performances were observed using TwT and 0.10Pd-
440 TwT, reaching 90 ± 2% and 93 ± 2%, respectively, after 3 h of UV irradiation, highlighting
441 the positive effect of the addition of Tween 80 during the synthesis.
442 The results showed the inhibitory effect of AHA, as observed for similar photocatalysts
443 [38,39]. According to Ye and coworkers, the inhibitory effect of NOM in the photocatalytic
444 degradation of pollutants can be attributed to three important facts. (i) The NOM present in
445 water matrices would reduce the availability of UV light for TiO_2 ("inner UV filter" effect). (ii)
446 NOM can act as scavenger of $^{\cdot}OH$ and h^+. (iii) NOM can hinder the target pollutant
447 degradation by competitive adsorption on the TiO_2 surface [35].
448 AHA (20 mg L^{-1}) in water at pH 7.0 shows a high absorption of light at wavelengths below
449 400 nm [74], demonstrating that the "inner UV filter" effect would be very relevant for
450 materials that do not absorb light below 400 nm. For our setup, the photolysis of the aqueous
451 solution of $[AHA]_0$ = 12 mg L^{-1} under UV lamps after 3 h presented a 29% decrease in the
452 total carbon content, showing the photodegradation of AHA, as reported [75]. Owing to their
453 absorption band between 450 and 600 nm, materials containing Pd could overcome the
454 "inner UV filter" effect.
455 Several authors reported the $^{\cdot}OH$ radical as the main oxidant in aqueous solution for TiO_2-
456 based photocatalysts [30,31,33,34,76]. The rate constant reported for the reaction between
457 AHA and $^{\cdot}OH$ radicals is 1.3 10^8 M_C^{-1} s^{-1} [76], where M_C is the molar concentration of carbon.
458 The analogous parameter for phenol is 1.1 10^9 M_C^{-1} s^{-1} (calculated from the rate constant
459 for the reaction of phenol and $^{\cdot}OH$ reported by Lindsey and coworkers: 6.6 10^9 M^{-1} s^{-1} [37]).
460 The slight difference, only of one order, indicates the importance of this reaction in the
461 degradation of phenol mediated by $^{\cdot}OH$ radicals. On the other hand, it was reported that
462 only the adsorbed fraction of AHA acts as a h^+ trap [77]. About AHA adsorption on the
463 photocatalyst surface, under the conditions studied, 20% of the initial amount of AHA was
464 adsorbed on 0.10Pd-T after 3 h of contact.
465 Then, all three aspects of the interference of AHA must be considered in the performance
466 of the synthesized materials under our experimental setup.
467 However, in all experiments, the total carbon content in the reaction mixture decreased,
468 reaching 36 ± 2%, 36 ± 2%, and 69 ± 2%, using T, TwT, and 0.10Pd-TwT, respectively.

These values indicated that the degree of mineralization of the reaction mixture included phenol, AHA, and by-products from phenol and AHA degradation. Then, the photocatalyst activated by UV irradiation was able to degrade phenol but also to destroy other organic compounds present in the reaction mixture. It should be highlighted that the mineralization reached a value as high as 69 ± 2% with 0.10Pd-TwT, evidencing the potential of this material as an efficient photocatalyst.

Considering the prospective use of solar irradiation, tests using visible lamps were carried out. Phenol photocatalytic degradation in the presence of AHA was tested with TwT or 0.10Pd-TwT (**Figure 9**). The ability of 0.10Pd-TwT to absorb visible light was demonstrated by the highest degradation observed: 67 ± 2% (versus 30 ± 2% with TwT). These results indicated that the material synthesized using Pd^{2+} and Tween 80, 0.10Pd-TwT was useful under both UV and visible light, being a promising photocatalyst for solar irradiation experiments.

The time evolution of phenol concentration in the presence of AHA under solar exposure was studied using 0.10Pd-TwT (**Figure 10**). The total irradiance incident on the systems ($H^{S}_{UV+VIS+NIR,T}$) after 5 h was 15206 kJ m^{-2} (this value includes 5% of UV irradiation). The percentage of phenol degradation with each photocatalyst is presented in **Table 3**.

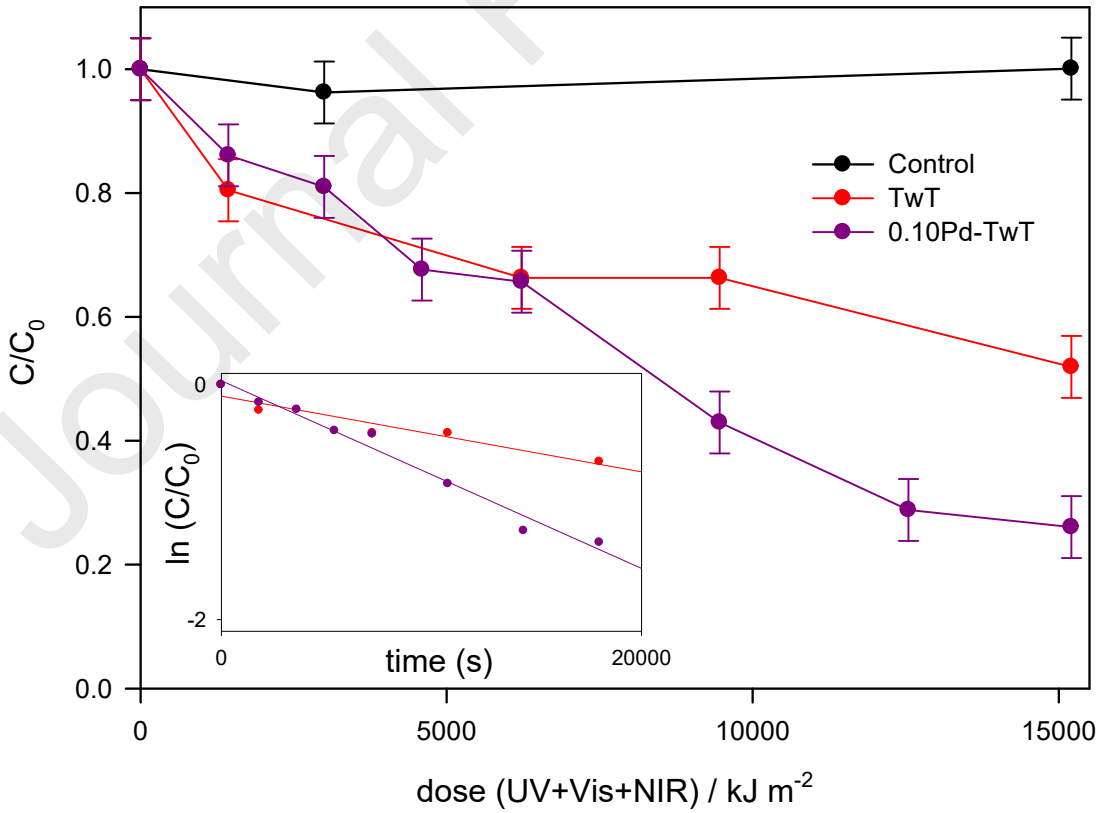

Figure 10. Time evolution of phenol concentration in the presence of humic acid (AHA), by solar exposure for 5 h, using TwT or 0.10Pd-TwT (1 g L^{-1} catalyst). A control assay without

catalyst is also included. $[phenol]_0$= 250 μM, $[AHA]_0$= 12 mg L^{-1}. Inset: Determination of apparent first order rate constants.

Table 3 Percentage degradation of phenol, percentage mineralization of reaction mixture, and apparent first order rate constant, for the solar exposure experiment. $[phenol]_0$= 250 μM; $[AHA]_0$= 12 mg L^{-1}; $[TC]_0$= 38 ppm_C; 1 g L^{-1} catalyst; 5 h; $H^S_{UV+VIS+NIR,T}$= 15206 kJ m^{-2}.

	Phenol degradation (%)	Mineralization (%)	Apparent k (s^{-1})
Control*	0 ± 2	28 ± 2	-
TwT	48 ± 2	63 ± 2	(3.2 ± 0.5) 10^{-5}
0.10Pd-TwT	74 ± 2	70 ± 2	(8.0 ± 0.5) 10^{-5}

*: without catalyst

The use of 0.10Pd-TwT allowed the degradation of 74 ± 2% of phenol (in the presence of AHA), which was higher than when using TwT (48 ± 2%), as expected for the solar spectrum. The control assay without catalyst indicated that direct photolysis was irrelevant. To estimate the global evolution of the carbon content throughout the reaction, the percentage of mineralization was determined. The control experiment showed 28 ± 2% of mineralization that could be assigned to AHA photodegradation, as discussed above. The presence of heterogeneous photocatalysts improved the mineralization, along with phenol degradation. The great performance of 0.10Pd-TwT, which reached 70 ± 2% of mineralization after 5 h of solar exposure, should be noted.

Additionally, to evaluate the possible metal leaching during the reaction, the palladium concentration in the mixture reaction was determined after the solar experiment with 0.10Pd-TwT. The value obtained was (2.7 ± 0.2) ppb Pd, below the local legal limit (5 ppm).

4. *Conclusions*

The presence of Pd^{2+} and Tween 80 during the sol-gel synthesis allowed obtaining a modified TiO_2 photocatalyst with great performance under UV and visible irradiation. This material was able to efficiently degrade phenol, even with the addition of humic acid to the reaction mixture. The solar irradiation experiment also showed excellent performance for 0.10Pd-TwT: 74% of phenol degradation after 5 h of exposure, with AHA as a ubiquitous interference.

The observed degradation of phenol along with mineralization and the neglected leaching of Pd indicated that the use of 0.10Pd-TwT activated by natural sunlight is a promising

approach for pollutant abatement, as an environmentally friendly and cost-effective alternative.

Acknowledgements

JAR, PIV and PC are research members of CONICET, Argentina. LR thanks CONICET for the fellowships. This research was supported by grant PIP 1522 from CONICET, PICT-2016-0372 and X835 from UNLP. The authors thank Alberto Caneiro from Y-TEC (La Plata, Argentina) for the TEM measurements and Alexis Sosa from CINDECA for the FTIR determinations. LMPM acknowledges the MICIN/AEI/10.13039/501100011033 and FSE "El FSE invierte en tu futuro" for the Ramón y Cajal research contract (RYC-2016-19347) and FEDER/Junta de Andalucía-Consejería de Transformación Económica, Industria, Conocimiento y Universidades/B-RNM-486-UGR20.

References

[1] K. Wetchakun, N. Wetchakun, S. Sakulsermsuk, An overview of solar/visible light-driven heterogeneous photocatalysis for water purification: TiO2- and ZnO-based photocatalysts used in suspension photoreactors, J. Ind. Eng. Chem. 71 (2019) 19–49. https://doi.org/10.1016/j.jiec.2018.11.025.

[2] C. Byrne, G. Subramanian, S.C. Pillai, Recent advances in photocatalysis for environmental applications, J. Environ. Chem. Eng. 6 (2018) 3531–3555. https://doi.org/10.1016/j.jece.2017.07.080.

[3] D. Chen, Y. Cheng, N. Zhou, P. Chen, Y. Wang, K. Li, S. Huo, P. Cheng, P. Peng, R. Zhang, L. Wang, H. Liu, Y. Liu, R. Ruan, Photocatalytic degradation of organic pollutants using TiO2-based photocatalysts: A review, J. Clean. Prod. 268 (2020) 121725. https://doi.org/10.1016/j.jclepro.2020.121725.

[4] M.R.D. Khaki, M.S. Shafeeyan, A.A.A. Raman, W.M.A.W. Daud, Application of doped photocatalysts for organic pollutant degradation - A review, J. Environ. Manage. 198 (2017) 78–94. https://doi.org/10.1016/j.jenvman.2017.04.099.

[5] K. Wenderich, G. Mul, Methods, Mechanism, and Applications of Photodeposition in Photocatalysis: A Review, Chem. Rev. 116 (2016) 14587–14619. https://doi.org/10.1021/acs.chemrev.6b00327.

[6] J. Low, J. Yu, M. Jaroniec, S. Wageh, A.A. Al-Ghamdi, Heterojunction Photocatalysts, Adv. Mater. 29 (2017) 1–20. https://doi.org/10.1002/adma.201601694.

[7] C.J. Huang, F.M. Pan, I.C. Chang, Enhanced photocatalytic decomposition of

methylene blue by the heterostructure of PdO nanoflakes and TiO 2 nanoparticles, Appl. Surf. Sci. 263 (2012) 345–351. https://doi.org/10.1016/j.apsusc.2012.09.058.

[8] W. Zhou, Y. Guan, D. Wang, X. Zhang, D. Liu, H. Jiang, J. Wang, X. Liu, H. Liu, S. Chen, PdO/TiO2 and Pd/TiO2 heterostructured nanobelts with enhanced photocatalytic activity, Chem. - An Asian J. 9 (2014) 1648–1654. https://doi.org/10.1002/asia.201301638.

[9] A.N. Banerjee, N. Hamnabard, S.W. Joo, A comparative study of the effect of Pd-doping on the structural, optical, and photocatalytic properties of sol–gel derived anatase TiO2 nanoparticles, Ceram. Int. 42 (2016) 12010–12026. https://doi.org/10.1016/j.ceramint.2016.04.128.

[10] Y. Xu, C. Zhang, L. Zhang, X. Zhang, H. Yao, J. Shi, Pd-catalyzed instant hydrogenation of TiO2 with enhanced photocatalytic performance, Energy Environ. Sci. 9 (2016) 2410–2417. https://doi.org/10.1039/c6ee00830e.

[11] S. Veziroglu, J. Hwang, J. Drewes, I. Barg, J. Shondo, T. Strunskus, O. Polonskyi, F. Faupel, O.C. Aktas, PdO nanoparticles decorated TiO2 film with enhanced photocatalytic and self-cleaning properties, Mater. Today Chem. 16 (2020). https://doi.org/10.1016/j.mtchem.2020.100251.

[12] C.H. Nguyen, C.C. Fu, R.S. Juang, Degradation of methylene blue and methyl orange by palladium-doped TiO2 photocatalysis for water reuse: Efficiency and degradation pathways, J. Clean. Prod. 202 (2018) 413–427. https://doi.org/10.1016/j.jclepro.2018.08.110.

[13] D. Selishchev, D. Svintsitskiy, L. Kovtunova, E. Gerasimov, A. Gladky, D. Kozlov, Surface modification of TiO2 with Pd nanoparticles for enhanced photocatalytic oxidation of benzene micropollutants, Colloids Surfaces A Physicochem. Eng. Asp. 612 (2021) 125959. https://doi.org/10.1016/j.colsurfa.2020.125959.

[14] H. Lee, M. Shin, M. Lee, Y.J. Hwang, Photo-oxidation activities on Pd-doped TiO2 nanoparticles: Critical PdO formation effect, Appl. Catal. B Environ. 165 (2015) 20–26. https://doi.org/10.1016/j.apcatb.2014.09.061.

[15] D.S. García-Zaleta, J. a. Montes De Oca-Valero, A.M. Torres-Huerta, M. a. Domínguez-Crespo, H.J. Dorantes-Rosales, R. López-González, A. García-Murillo, Effect of Pd Addition on the Nanostructure and Properties of Pd/TiO2 Catalysts for the Photocatalytic Degradation of 4-Chlorophenol, J. Nano Res. 28 (2014) 9–20. https://doi.org/10.4028/www.scientific.net/JNanoR.28.9.

[16] M. Kirilov, B. Koumanova, L. Spasov, L. Petrov, Effects of Ag and Pd modifications of TiO2 on the photocatalytic degradation of p-chlorophenol in aqueous solution, Chem.

Technol. (2006) 343–348.

[17] S. Jin, F. Shiraishi, Photocatalytic activities enhanced for decompositions of organic compounds over metal-photodepositing titanium dioxide, Chem. Eng. J. 97 (2004) 203–211. https://doi.org/10.1016/j.cej.2003.04.001.

[18] B. Mazinani, N.M. Zalani, M. Sakaki, K. Yanagisawa, Hydrothermal synthesis of mesoporous TiO2–ZnO nanocomposite for photocatalytic degradation of methylene blue under UV and visible light, J. Mater. Sci. Mater. Electron. 29 (2018) 11945–11950. https://doi.org/10.1007/s10854-018-9296-5.

[19] J. Yuenyongsuwan, N. Nithiyakorn, P. Sabkird, E.A. O'Rear, T. Pongprayoon, Surfactant effect on phase-controlled synthesis and photocatalyst property of TiO2 nanoparticles, Mater. Chem. Phys. 214 (2018) 330–336. https://doi.org/10.1016/j.matchemphys.2018.04.111.

[20] Y. Chen, D.D. Dionysiou, Bimodal mesoporous TiO2-P25 composite thick films with high photocatalytic activity and improved structural integrity, Appl. Catal. B Environ. 80 (2008) 147–155. https://doi.org/10.1016/j.apcatb.2007.11.010.

[21] M.S. Lee, S.S. Park, G.D. Lee, C.S. Ju, S.S. Hong, Synthesis of TiO2 particles by reverse microemulsion method using nonionic surfactants with different hydrophilic and hydrophobic group and their photocatalytic activity, Catal. Today. 101 (2005) 283–290. https://doi.org/10.1016/j.cattod.2005.03.018.

[22] M.L. García-Benjume, M.I. Espitia-Cabrera, M.E. Contreras-García, Hierarchical macro-mesoporous structures in the system TiO2-Al2O3, obtained by hydrothermal synthesis using Tween-20® as a directing agent, Mater. Charact. 60 (2009) 1482–1488. https://doi.org/10.1016/j.matchar.2009.08.003.

[23] H. Choi, E. Stathatos, D.D. Dionysiou, Synthesis of nanocrystalline photocatalytic TiO2 thin films and particles using sol-gel method modified with nonionic surfactants, Thin Solid Films. 510 (2006) 107–114. https://doi.org/10.1016/j.tsf.2005.12.217.

[24] A. Zakersalehi, M. Nadagouda, H. Choi, Suppressing NOM access to controlled porous TiO2 particles enhances the decomposition of target water contaminants, Catal. Commun. 41 (2013) 79–82. https://doi.org/10.1016/j.catcom.2013.07.013.

[25] I. Ibrahim, G. V Belessiotis, M.K. Arfanis, C. Athanasekou, A.I. Philippopoulos, C.A. Mitsopoulou, G.E. Romanos, P. Falaras, Surfactant E ff ects on the Synthesis of Redox Photocatalysts, Bifunctional V2 O5 Photocatalysts, (2020).

[26] M. Maicu, M.C. Hidalgo, G. Colón, J.A. Navío, Comparative study of the photodeposition of Pt, Au and Pd on pre-sulphated TiO2 for the photocatalytic decomposition of phenol, J. Photochem. Photobiol. A Chem. 217 (2011) 275–283.

https://doi.org/10.1016/j.jphotochem.2010.10.020.
[27] Y. Wang, L. Zhou, X. Duan, H. Sun, E.L. Tin, W. Jin, S. Wang, Photochemical degradation of phenol solutions on Co3O4 nanorods with sulfate radicals, Catal. Today. 258 (2015) 576–584. https://doi.org/10.1016/j.cattod.2014.12.020.
[28] L. Duan, S. Rao, D. Wang, K. Zhang, H. Cao, Z. Liu, Q. Guo, W. Li, J. Tao, Y. Gao, Understanding of TiO2 catalysis mechanism in underwater pulsed discharge system: Charge carrier generation and interfacial charge-transfer processes, Chemosphere. 267 (2021) 129249. https://doi.org/10.1016/j.chemosphere.2020.129249.
[29] T. Olmez-Hanci, I. Arslan-Alaton, Comparison of sulfate and hydroxyl radical based advanced oxidation of phenol, Chem. Eng. J. 224 (2013) 10–16. https://doi.org/10.1016/j.cej.2012.11.007.
[30] V. Diesen, M. Jonsson, Formation of H 2 O 2 in TiO 2 photocatalysis of oxygenated and deoxygenated aqueous systems: A probe for photocatalytically produced hydroxyl radicals, J. Phys. Chem. C. 118 (2014) 10083–10087. https://doi.org/10.1021/jp500315u.
[31] J. Schneider, M. Matsuoka, M. Takeuchi, J. Zhang, Y. Horiuchi, M. Anpo, D.W. Bahnemann, Understanding TiO2photocatalysis: Mechanisms and materials, Chem. Rev. 114 (2014) 9919–9986. https://doi.org/10.1021/cr5001892.
[32] M. V Martin, P.I. Villabrille, J.A. Rosso, The influence of Ce doping of titania on the photodegradation of phenol, Environ. Sci. Pollut. Res. (2015) 14291–14298. https://doi.org/10.1007/s11356-015-4667-4.
[33] M. Sillanpää, M.C. Ncibi, A. Matilainen, Advanced oxidation processes for the removal of natural organic matter from drinking water sources: A comprehensive review, J. Environ. Manage. 208 (2018) 56–76. https://doi.org/10.1016/j.jenvman.2017.12.009.
[34] D.C.A. Gowland, N. Robertson, E. Chatzisymeon, Photocatalytic oxidation of natural organic matter-fulvic acid in water, Water. 13 (2021) 288. https://doi.org/https://doi.org/10.3390/ w13030288.
[35] Y. Ye, H. Bruning, W. Liu, H. Rijnaarts, D. Yntema, Effect of dissolved natural organic matter on the photocatalytic micropollutant removal performance of TiO2 nanotube array, J. Photochem. Photobiol. A Chem. 371 (2019) 216–222. https://doi.org/10.1016/j.jphotochem.2018.11.012.
[36] Y. Ye, Y. Feng, H. Bruning, D. Yntema, H.H.M. Rijnaarts, Photocatalytic degradation of metoprolol by TiO2 nanotube arrays and UV-LED: Effects of catalyst properties, operational parameters, commonly present water constituents, and photo-induced reactive species, Appl. Catal. B Environ. 220 (2018) 171–181.

https://doi.org/10.1016/j.apcatb.2017.08.040.
[37] M.E. Lindsey, M.A. Tarr, Inhibition of hydroxyl radical reaction with aromatics by dissolved natural organic matter, Environ. Sci. Technol. 34 (2000) 444–449. https://doi.org/10.1021/es990457c.
[38] M. Palacio, L. Rossi, E.M. Farías Hermosilla, J.A. Rosso, P.I. Villabrille, M. V. Martin, Selective photodegradation of phenol in the presence of a commercial humic acid, J. Environ. Chem. Eng. 5 (2017) 5540–5546. https://doi.org/10.1016/j.jece.2017.10.021.
[39] L. Rossi, M. Palacio, P.I. Villabrille, J.A. Rosso, V-doped TiO2 photocatalysts and their application to pollutant degradation, Environ. Sci. Pollut. Res. 28 (2021) 24112–24123. https://doi.org/10.1007/s11356-021-12339-5.
[40] T.E. Doll, F.H. Frimmel, Photocatalytic degradation of carbamazepine, clofibric acid and iomeprol with P25 and Hombikat UV100 in the presence of natural organic matter (NOM) and other organic water constituents, Water Res. 39 (2005) 403–411. https://doi.org/10.1016/j.watres.2004.09.016.
[41] T.E. Doll, F.H. Frimmel, Removal of selected persistent organic pollutants by heterogeneous photocatalysis in water, Catal. Today. 101 (2005) 195–202. https://doi.org/10.1016/j.cattod.2005.03.005.
[42] M.V. Martin, A. Ipiña, P.I. Villabrille, J.A. Rosso, Combination of sunlight, oxidants, and Ce-doped TiO2 for phenol degradation, Environ. Sci. Pollut. Res. 24 (2017). https://doi.org/10.1007/s11356-016-6258-4.
[43] H.P. Klug, L.E. Alexander, X-Ray Diffraction Procedures: For Polycrystalline and Amorphous Materials, 1974.
[44] O. Wiranwetchayan, S. Promnopat, T. Thongtem, A. Chaipanich, S. Thongtem, Effect of polymeric precursors on the properties of TiO2 films prepared by sol-gel method, Mater. Chem. Phys. 240 (2020) 122219. https://doi.org/10.1016/j.matchemphys.2019.122219.
[45] A. Zielińska-Jurek, J. Hupka, Preparation and characterization of Pt/Pd-modified titanium dioxide nanoparticles for visible light irradiation, Catal. Today. 230 (2014) 181–187. https://doi.org/10.1016/j.cattod.2013.09.045.
[46] Q. Zhao, H. Li, L. Zhang, Y. Cao, Study of PdO species on surface of TiO2 for photoreduction of CO2 into CH4, J. Photochem. Photobiol. A Chem. 384 (2019) 112032. https://doi.org/10.1016/j.jphotochem.2019.112032.
[47] M. Thommes, K. Kaneko, A. V. Neimark, J.P. Olivier, F. Rodriguez-Reinoso, J. Rouquerol, K.S.W. Sing, Physisorption of gases, with special reference to the evaluation of surface area and pore size distribution (IUPAC Technical Report), Pure

Appl. Chem. 87 (2015) 1051–1069. https://doi.org/10.1515/pac-2014-1117.
[48] K.A. Cychosz, R. Guillet-Nicolas, J. García-Martínez, M. Thommes, Recent advances in the textural characterization of hierarchically structured nanoporous materials, Chem. Soc. Rev. 46 (2017) 389–414. https://doi.org/10.1039/c6cs00391e.
[49] S. Sakthivel, H. Kisch, Daylight Photocatalysis by Carbon-Modified Titanium Dioxide, Angew. Chemie - Int. Ed. 42 (2003) 4908–4911. https://doi.org/10.1002/anie.200351577.
[50] X. Han, L. An, Y. Hu, Y. Li, C. Hou, H. Wang, Q. Zhang, Ti3C2 MXene-derived carbon-doped TiO2 coupled with g-C3N4 as the visible-light photocatalysts for photocatalytic H2 generation, Appl. Catal. B Environ. 265 (2020) 118539. https://doi.org/10.1016/j.apcatb.2019.118539.
[51] W. Ren, Z. Ai, F. Jia, L. Zhang, X. Fan, Z. Zou, Low temperature preparation and visible light photocatalytic activity of mesoporous carbon-doped crystalline TiO2, Appl. Catal. B Environ. 69 (2007) 138–144. https://doi.org/10.1016/j.apcatb.2006.06.015.
[52] J. Zhong, F. Chen, J. Zhang, Carbon-deposited TiO2: Synthesis, characterization, and visible photocatalytic performance, J. Phys. Chem. C. 114 (2010) 933–939. https://doi.org/10.1021/jp909835m.
[53] J. Liu, L. Han, N. An, L. Xing, H. Ma, L. Cheng, J. Yang, Q. Zhang, Enhanced visible-light photocatalytic activity of carbonate-doped anatase TiO2 based on the electron-withdrawing bidentate carboxylate linkage, Appl. Catal. B Environ. 202 (2017) 642–652. https://doi.org/10.1016/j.apcatb.2016.09.057.
[54] J. Yan, X. Li, B. Jin, M. Zeng, R. Peng, Synthesis of TiO2/Pd and TiO2/PdO Hollow Spheres and Their Visible Light Photocatalytic Activity, Int. J. Photoenergy. 2020 (2020). https://doi.org/10.1155/2020/4539472.
[55] Y. Yan, Y. Yu, S. Huang, Y. Yang, X. Yang, S. Yin, Y. Cao, Adjustment and Matching of Energy Band of TiO2-Based Photocatalysts by Metal Ions (Pd, Cu, Mn) for Photoreduction of CO2 into CH4, J. Phys. Chem. C. 121 (2017) 1089–1098. https://doi.org/10.1021/acs.jpcc.6b07180.
[56] L. Shi, Q. Han, L. Cao, F. Zhao, C. Xia, B. Dong, Y. Xi, A novel ammonia complex-assisted ion-exchange strategy to fabricate heterostructured PdO/TiO2 nanorods with enhanced photocatalytic activities, J. Nanoparticle Res. 18 (2016) 1–10. https://doi.org/10.1007/s11051-016-3670-0.
[57] Z. Wu, Z. Sheng, Y. Liu, H. Wang, N. Tang, J. Wang, Characterization and activity of Pd-modified TiO 2 catalysts for photocatalytic oxidation of NO in gas phase, J. Hazard. Mater. 164 (2009) 542–548. https://doi.org/10.1016/j.jhazmat.2008.08.028.

[58] A.H. Keihan, H. Rasouli-nezhad, A. Mohammadgholi, S. Sajjadi, R. Hosseinzadeh, M. Farhadian, G. Hosseinzadeh, Pd nanoparticle loaded TiO2 semiconductor for photocatalytic degradation of Paraoxon pesticide under visible-light irradiation, J. Mater. Sci. Mater. Electron. 28 (2017) 16718–16727. https://doi.org/10.1007/s10854-017-7585-z.

[59] M. V. Martin, P.I. Villabrille, J.A. Rosso, The influence of Ce doping of titania on the photodegradation of phenol, Environ. Sci. Pollut. Res. 22 (2015) 14291–14298. https://doi.org/10.1007/s11356-015-4667-4.

[60] K. Das, S.N. Sharma, M. Kumar, S.K. De, Morphology dependent luminescence properties of Co doped TiO2 nanostructures, J. Phys. Chem. C. 113 (2009) 14783–14792. https://doi.org/10.1021/jp9048956.

[61] M.V. Dozzi, A. Candeo, G. Marra, C. D'Andrea, G. Valentini, E. Selli, Effects of Photodeposited Gold vs Platinum Nanoparticles on N,F-Doped TiO2 Photoactivity: A Time-Resolved Photoluminescence Investigation, J. Phys. Chem. C. 122 (2018) 14326–14335. https://doi.org/10.1021/acs.jpcc.8b02997.

[62] H.S. Bae, M.A. Mahadik, Y.S. Seo, W.S. Chae, H.S. Chung, H.I. Ryu, M. Cho, P.J. Shea, S.H. Choi, J.S. Jang, Palladium metal oxide/hydroxide clustered cobalt oxide co-loading on acid treated TiO2 nanorods for degradation of organic pollutants and Salmonella typhimurium inactivation under simulated solar light, Chem. Eng. J. 408 (2021) 127260. https://doi.org/10.1016/j.cej.2020.127260.

[63] P. Weerachawanasak, G.J. Hutchings, J.K. Edwards, S.A. Kondrat, P.J. Miedziak, P. Prasertham, J. Panpranot, Surface functionalized TiO2 supported Pd catalysts for solvent-free selective oxidation of benzyl alcohol, Catal. Today. 250 (2015) 218–225. https://doi.org/10.1016/j.cattod.2014.06.005.

[64] X. Chen, Y. Huang, H. Li, Y. Li, X. Wang, X. Zhu, X. Xu, Assessment of CO2 photoconversion over TiO2/La2O3 treated with acetic acid, Mater. Lett. 303 (2021) 130466. https://doi.org/10.1016/j.matlet.2021.130466.

[65] The Materials Project, Lawrence Berkeley National Laboratory. University of California., (n.d.). https://materialsproject.org/materials/mp-1336/.

[66] K. Ye, Y. Li, H. Yang, M. Li, Y. Huang, S. Zhang, H. Ji, An ultrathin carbon layer activated CeO2 heterojunction nanorods for photocatalytic degradation of organic pollutants, Appl. Catal. B Environ. 259 (2019). https://doi.org/10.1016/j.apcatb.2019.118085.

[67] M. Zhou, M. Li, C. Hou, Z. Li, Y. Wang, K. Xiang, X. Guo, Pt nanocrystallines/TiO2 with thickness-controlled carbon layers: Preparation and activities in CO oxidation,

Chinese Chem. Lett. 29 (2018) 787–790. https://doi.org/10.1016/j.cclet.2018.03.010.
[68] J.H. Yu, S.H. Nam, J.W. Lee, D.I. Kim, J.H. Boo, Oxidation state and structural studies of vanadium-doped titania particles for the visible light-driven photocatalytic activity, Appl. Surf. Sci. 472 (2019) 46–53. https://doi.org/10.1016/j.apsusc.2018.04.125.
[69] L.S. Kibis, A.I. Titkov, A.I. Stadnichenko, S. V. Koscheev, A.I. Boronin, X-ray photoelectron spectroscopy study of Pd oxidation by RF discharge in oxygen, Appl. Surf. Sci. 255 (2009) 9248–9254. https://doi.org/10.1016/j.apsusc.2009.07.011.
[70] O. Lupan, V. Postica, M. Hoppe, N. Wolff, O. Polonskyi, T. Pauporté, B. Viana, O. Majérus, L. Kienle, F. Faupel, R. Adelung, PdO/PdO2 functionalized ZnO:::Pd films for lower operating temperature H2 gas sensing, Nanoscale. 10 (2018) 14107–14127. https://doi.org/10.1039/c8nr03260b.
[71] X.G. Zhao, L.Q. Huang, Iridium, carbon and nitrogen multiple-doped TiO2 Nanoparticles with enhanced photocatalytic activity, Ceram. Int. 43 (2017) 3975–3980. https://doi.org/10.1016/j.ceramint.2016.11.083.
[72] X. Liu, A. Jin, Y. Jia, T. Xia, C. Deng, M. Zhu, C. Chen, X. Chen, Synergy of adsorption and visible-light photocatalytic degradation of methylene blue by a bifunctional Z-scheme heterojunction of WO 3 /g-C 3 N 4, Appl. Surf. Sci. 405 (2017) 359–371. https://doi.org/10.1016/j.apsusc.2017.02.025.
[73] A.A. Ismail, Mesoporous PdO-TiO 2 nanocomposites with enhanced photocatalytic activity, Appl. Catal. B Environ. 117–118 (2012) 67–72. https://doi.org/10.1016/j.apcatb.2012.01.006.
[74] L. Carlos, D.O. Mártire, M.C. Gonzalez, J. Gomis, A. Bernabeu, A.M. Amat, A. Arques, Photochemical fate of a mixture of emerging pollutants in the presence of humic substances, Water Res. 46 (2012) 4732–4740. https://doi.org/10.1016/j.watres.2012.06.022.
[75] G.N. Bosio, P.D. Gara, F.S.G. Einschlag, M.C. Gonzalez, M.T. Del Panno, D.O. Mártire, Photodegradation of soil organic matter and its effect on gram-negative bacterial growth, Photochem. Photobiol. 84 (2008) 1126–1132. https://doi.org/10.1111/j.1751-1097.2007.00274.x.
[76] T.M. Hwang, S.H. Nam, J. Lee, J.W. Koo, E. Kim, M. Kwon, Hydroxyl radical scavenging factor measurement using a fluorescence excitation-emission matrix and parallel factor analysis in ultraviolet advanced oxidation processes, Chemosphere. 259 (2020) 127396. https://doi.org/10.1016/j.chemosphere.2020.127396.
[77] X. Yan, R. Bao, S. Yu, Q. Li, Q. Jing, The roles of hydroxyl radicals, photo-generated holes and oxygen in the photocatalytic degradation of humic acid, Russ. J. Phys.

Chem. A: 86 (2012) 1479–1485. https://doi.org/10.1134/S0036024412070333.

Graphical abstract

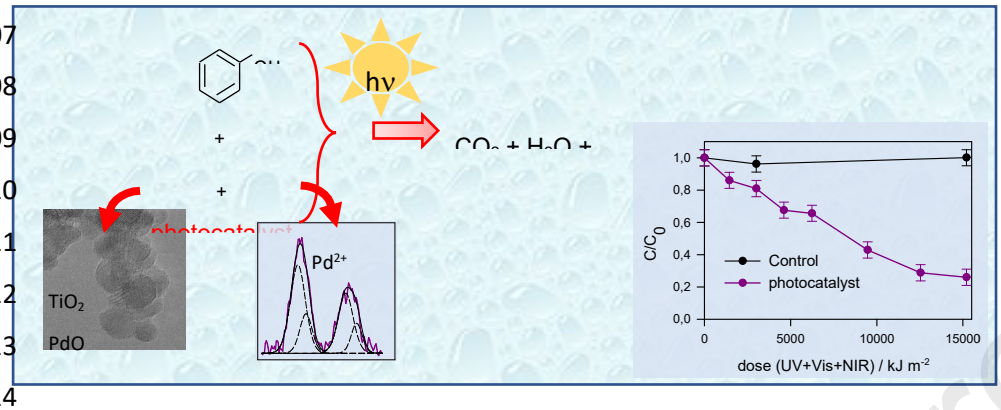

Highlights

- TiO_2 photocatalysts synthesized by the sol-gel method with Pd^{2+} ions and Tween 80
- Selective degradation of phenol in the presence of humic acid as interference
- Solar radiation experiment showed excellent performance